Journal of
Synchrotron
Radiation

ISSN 0909-0495

Received 8 June 2011
Accepted 2 November 2011

Global and local hard X-ray tomography of a centimeter-size tumor vessel tree

Sabrina Lang,[a] Marco Dominietto,[b] Philippe Cattin,[c] Alexandra Ulmann-Schuler,[d] Timm Weitkamp[e] and Bert Müller[a]*

[a]Biomaterials Science Center, University of Basel, 4031 Basel, Switzerland, [b]Institute for Biomedical Engineering, ETH Zürich, 8093 Zürich, Switzerland, [c]Medical Image Analysis Center, University of Basel, 4031 Basel, Switzerland, [d]Institute of Zoology, University of Zürich, 8057 Zürich, Switzerland, and [e]Synchrotron Soleil, 91190 Gif-sur-Yvette, France.
E-mail: bert.mueller@unibas.ch

The visualization of the vascular network in tumors down to the smallest vessels requires high spatial resolution and reasonable contrast. Stained corrosion casts of the microvasculature network guarantee superior X-ray absorption contrast and highest reproduction fidelity. Tomography of a centimeter-size tumor, however, is unfeasible at the spatial resolution needed to reveal the smallest vessels. Therefore, local tomography has been performed to visualize the smallest capillaries within the region of interest. These three-dimensional data show the detailed morphology, but the reconstructed absorption coefficients obtained in local tomography differ substantially from the absorption coefficients retrieved from the less detailed global tomography data. This paper deals with the adaptation of local tomography data using the global data and considers two-parameter histogram matching of the radiographs, sinogram extension, and multi-parameter cupping correction. It is demonstrated that two-parameter histogram matching of the radiographs already provides reasonable agreement. The change of the lens in front of the detector's camera, however, significantly affects the obtained local X-ray absorption coefficients in the tomograms predominantly owing to the dissimilar point-spread functions of the two configurations used, and much less to the fact that one of the data sets was acquired in a local geometry.

Keywords: synchrotron-radiation-based micro-computed tomography; local tomography; lens-coupled CCD; tumor vascularization; angiogenesis; histogram matching.

1. Introduction

Cancer is a leading cause of death worldwide (WHO, 2009). A lot of studies in cancer research investigate the neo-vascularization in cancerous tissue to obtain insight into tumor formation and growth (Müller *et al.*, 2008) with the aim of developing strategies against the disease. For a detailed investigation of the underlying phenomena, a three-dimensional (3D) visualization of the tumor vessel tree down to the capillary level would be most helpful. The smallest capillaries in the tumors (of centimeter size) have a diameter of around 4 µm and a wall thickness of about 1 µm (Potter & Groom, 1983; Wiedeman, 1963). Synchrotron-radiation-based micro-computed tomography (SRµCT) reaches the submicrometer regime without X-ray optics (Takeda *et al.*, 1998; Haberthür *et al.*, 2010), but for the given resolution the field of view (FOV) is restricted. For specimens which exceed the FOV, one can only cut the specimen into pieces of appropriate size or use the stitching technique where the projections are recorded at different asymmetric rotation axes to obtain the entire projection images of the tumor for each rotation angle (Haberthür *et al.*, 2010; Müller *et al.*, 2007). These techniques are time-consuming because they require the acquisition of many more detector frames than a standard tomography scan. Moreover, the volume of the data tends to become huge, which results in long times needed for data reconstruction, and difficult management of the data. Consequently, many research teams only acquire a region of interest (ROI) of the entire projection and reconstruct just these partial datasets, an approach known as local tomography or truncated-projection tomography. In local tomography, however, the reconstructed X-ray absorption coefficients $\mu(x, y, z)$ do not correspond to the values obtained from globally acquired data (Haberthür *et al.*, 2010; Pfeiffer *et al.*, 2008; Faridani *et al.*, 1992; Gureyev *et al.*, 2007). The deviations, a result of the interior problem, can only be slightly evaded (Pfeiffer *et al.*, 2008) but not completely corrected (Köhler & Noo, 2009). Different algorithms have been reported to partially correct the related artifacts

(Bonnet *et al.*, 2000; Marone *et al.*, 2010). For cases in which the absorption coefficients are known *a priori* for a subset of the ROI to be reconstructed, the problem can be solved, but this requires iterative algorithms, which are relatively complex and computationally intensive (Kudo *et al.*, 2008).

The present work deals with the question of how far the local X-ray absorption coefficients $\mu(x, y, z)$ in the different local tomograms can be corrected using information from the less detailed global data. First, an attempt is made to shift and scale the binned μ values of the local data to obtain those of the global tomogram. Second, the artifacts in the local tomogram are reduced combining the high-resolution projections with less detailed data of the missing regions before reconstruction. Third, using the rigid or affine registration, the influence of distortions, for example, as the result of the objective's aberration, is addressed. Hence, the pros and cons of local tomography and the combination between local and global tomography are elucidated.

It should be noted that the corrosion cast of the tumor vessel tree is especially suitable for this kind of evaluation as only two components (polymer and air) are present and, therefore, the density resolution is not a limiting factor.

2. Methods and materials

2.1. Specimen preparation

Three BALB/c nude mice (Charles River Laboratories, France) were used for the experiments in strict adherence to the Swiss animal protection law. A suspension of 10^6 C51 tumor cells (murine colon carcinoma) was injected subcutaneously into the left flank of each animal. Ten days following injection, when the tumors reached an average diameter of about 10 mm, mice were sacrificed and perfused with a polyurethane-based material (Krucker *et al.*, 2006) in order to produce a corrosion cast of the whole circulatory system. The casted tumors were subsequently extracted and treated with OsO_4 to enhance the contrast in SRμCT. The tumor cast was fixed on the sample holder with wax, as shown in Fig. 1.

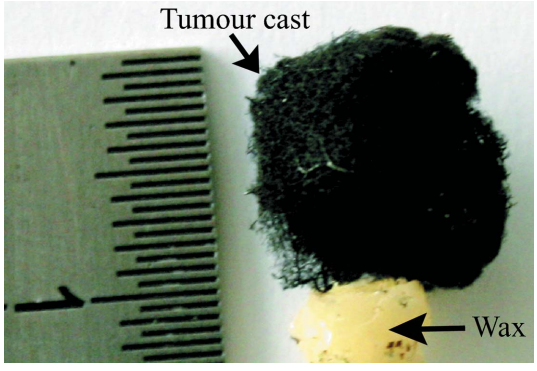

Figure 1
The photograph shows the corrosion cast of C51 tumor vessels grown in a nude mouse. The black color of the polyurethane cast results from the OsO_4 treatment. Wax served for fixation on the rotation stage for data acquisition.

2.2. Synchrotron-radiation-based micro-computed tomography

SRμCT measurements were performed at the TOMCAT beamline [Swiss Light Source (SLS), Paul Scherrer Institut, Villigen, Switzerland] in absorption contrast mode (Stampanoni *et al.*, 2006). A double-multilayer monochromator was used to select a photon energy of 15 keV. The tumor cast was fixed on the rotation stage to acquire 1500 projections in 0.12° steps between 0 and 180°. The high-resolution imaging detector is based on a 4.2 Mpixel CCD camera [PCO, Germany (PCO-AG, 2008), 2048 × 2048 pixels; 7.4 μm physical pixel size] coupled to the X-ray beam by a microscope lens system (Optique Peter, Lyon, France) and a 20 μm-thin single-crystal scintillator made of cerium-doped lutetium aluminium garnet (LAG:Ce) which converted the X-rays into visible light. The microscope objective determines the magnification and the actual effective pixel size on the specimen scale. In this experiment a PLAPO1.25X [numerical aperture (NA) 0.04] and a UPLAPO10X (NA 0.4) objective from the Olympus UIS series (Olympus Corporation, Tokyo, Japan) were used. Tomograms of the whole specimen were measured using the 1.25× objective; the effective nominal pixel size with this objective was 5.92 μm. The field of view of 12 mm for this set-up was sufficient to enclose the maximal diameter of the tumor. However, the pixel size was too large to discriminate between tiny capillaries and to extract their diameters. Six hours after the global measurements the set-up was changed to a 10× objective, giving a pixel size of 0.74 μm. The resulting FOV, however, is only 1.5 mm wide, which is substantially smaller than the tumor size. Therefore, this objective was only applied to perform local tomography. For both settings an exposure time of 0.175 s per radiograph was used. The global and local measurements were carried out each within approximately 5 min. The distance between the specimen and scintillator was estimated to be 2 mm for global and local data acquisition. This short distance was chosen to minimize the effect of edge-enhancing propagation-based phase contrast, although this phenomenon cannot be completely eliminated. At an X-ray wavelength of 0.83 Å, the characteristic width of phase-contrast fringes at this propagation distance is $(2\ \text{mm} \times 0.83\ \text{Å})^{1/2} = 0.4\ \mu\text{m}$. In the reconstructed tomograms, this leads to bright/dark fringe pairs, which broaden the histograms of the absorption coefficients. The distance between the camera and the scintillator was 30 cm whereby the scintillator-to-objective distance was 2–3 mm for the 0.04 objective lens and several 100 μm for the 0.4 objective lens.

2.3. Data analysis

2.3.1. Flat-field correction. Flat-field images were taken before and after the acquisition of the projection radiographs in each tomography scan. The mean intensity of the flat-field images taken before data acquisition was higher by 7.2% for the global and by 2.0% for the local data sets than those recorded after data acquisition. This can only partly be explained by variations of the electron beam current in the

source, because the top-up mode operation of the SLS keeps these variations at about 2%. We suspect darkening of the detector lens optics and/or thermal changes of the monochromator as the predominant reasons. In the radiographs measured with a pixel size of 5.92 µm there are areas without X-ray absorbing specimen, which allows the time-dependent decay of intensity to be extracted. This information was implemented into the flat-field correction of the radiographs. For the flat-field correction of the data acquired with a pixel size of 0.74 µm, the background images taken before and after the projection radiographs were interpolated linearly before flat-field normalization.

2.3.2. Reconstruction. The tomographic reconstruction of both the global and the local tomography data sets was performed using the filtered back-projection technique, implemented in the parallel-beam reconstruction software *PyHST* (European Synchrotron Radiation Facility, Grenoble, France) (Hammersley, 1999).

2.3.3. Projection analysis. The global and local projections were compared to determine potential differences between the two objectives. We term the projections *global* for the 5.92 µm pixel size and *local* for the 0.74 µm pixel size. For comparison the corresponding ROIs in the global and local projections were selected. Rigid registration based on similarity transform was carried out (see Fig. 2) to identify the same ROIs (common volume) in both images (Modersitzki, 2004). The software used for the registration was *MATLAB R2010a* and *Simulink* (Mathworks, Natwick, MA, USA). The similarity transformation in two dimensions includes the two translation parameters (t_x, t_y), uniform scaling (s) and one rotation parameter (φ),

$$\begin{pmatrix} x' \\ y' \end{pmatrix} = \begin{bmatrix} s\cos\varphi & -s\sin\varphi \\ s\sin\varphi & s\cos\varphi \end{bmatrix} \begin{pmatrix} x \\ y \end{pmatrix} + \begin{pmatrix} t_x \\ t_y \end{pmatrix}. \quad (1)$$

The coordinates x' and y' describe the transformed coordinates. The registration process implies that one image (the floating image) is transformed according to the reference image until optimal similarity is achieved for the similarity function. Here, the 'normalized mutual information' (NMI) was used as a similarity function, which allows the registration of images with different intensity distributions (Knops *et al.*, 2006). To obtain the NMI, first the joint histogram $h(a,b)$ of the two images had to be determined. The components consist of the X-ray absorption coefficients from the local image (a) and the absorption coefficients from the global image (b). The intensity values in the joint histogram correspond to the counts of the absorption-value combinations in the local and the global image, respectively. The values of the joint histogram (a,b) describe the number of joint pixels between the reference and floating images. When creating a joint histogram of identical images all values lie on a diagonal through the origin. From the joint histogram the probability density function $p(a,b)$ can be determined,

$$p(a, b) = (1/N)\, h(a, b), \quad (2)$$

where N is the number of values in the joint histogram. $p(a,b)$ describes the probability that two pixels in the reference and floating images with the same coordinate have intensity values a and b. Using $p(a,b)$, the Shannon–Wiener entropy H_{ab} could be determined,

$$H_{ab} = -\sum_{ab} p(a, b) \log[p(a, b)]. \quad (3)$$

The higher the similarity between two images, the lower is the Shannon–Wiener entropy. The NMI Y_{ab} is determined using the Shannon–Wiener entropy. The advantage of the NMI against the entropy is that it does not simply maximize the overlap of air,

$$Y_{ab} = (H_a + H_b)/H_{ab}. \quad (4)$$

The NMI maximizes at the optimal alignment and can be thought of as a measure of how well one image explains the other. For the preparation of the projections for the regis-

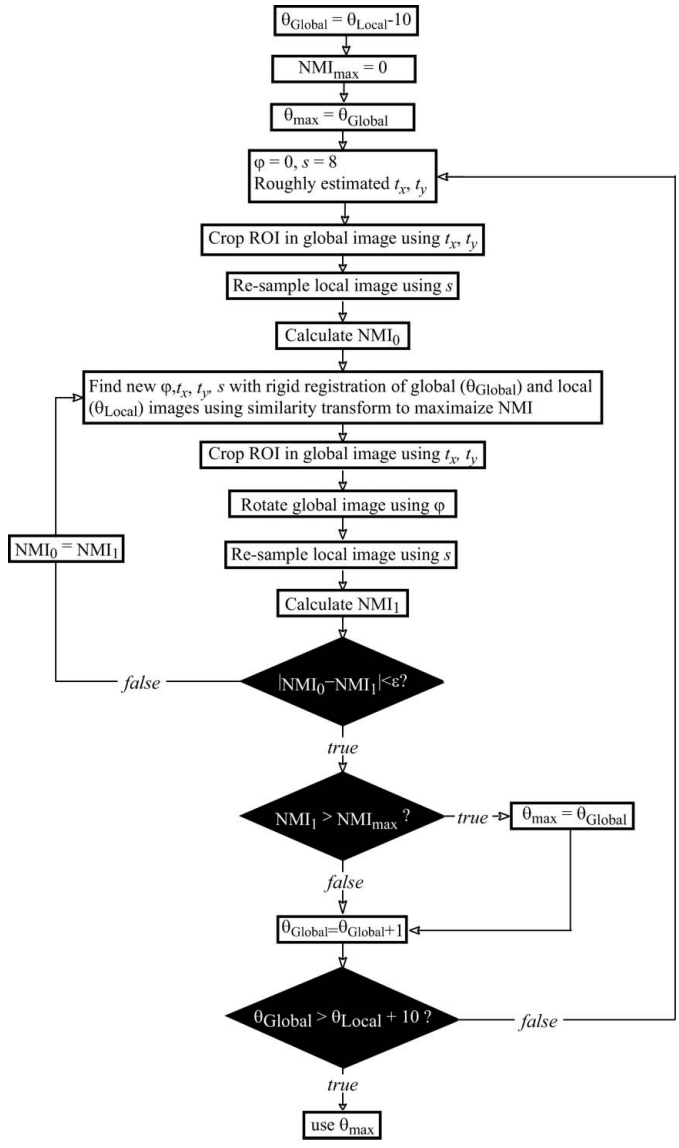

Figure 2
The registration procedure of local and global data is summarized in the flow diagram. θ describes the rotation angle step at which the projection was scanned. The local projections serve as a reference, the global projections as a floating image.

tration, a region that is seen in the global as well as in the local projections is manually cropped. The cropped region is defined to be the floating image. The reference image here was the local projection, which had been binned by a factor of eight, the nearest integer value to the scaling parameter, to obtain approximately the same number of pixels in both datasets. After registration the rotation and translation parameters were used to refine the cropping. The scaling parameter was applied to refine the re-sample factor for re-sizing the local projection. The registration was repeated using the optimized floating and reference images until maximal similarity between the images was achieved. A histogram was calculated from the cropped global and the re-scaled local projections to compare the intensity distribution of both images.

2.3.4. Tomogram analysis. Analogous to the projections, a 3D registration tool (Andronache *et al.*, 2008) for registering the tomography data was applied. The transformations were carried out along the *x*-, *y*- and *z*-axes so we obtained the translation parameters (t_x, t_y, t_z). The scaling depends here on three orthogonal directions. Hence, the three scaling parameters s_x, s_y and s_z were introduced. The histograms of the cropped global and the re-sampled local 3D datasets were determined.

2.3.5. Histogram analysis. Histograms characterize the contrast and density resolution of tomography data (Thurner *et al.*, 2004). Here, the peak positions and the related full width at half-maximum (FWHM) values were determined. The histograms of the global and local tomograms were compared.

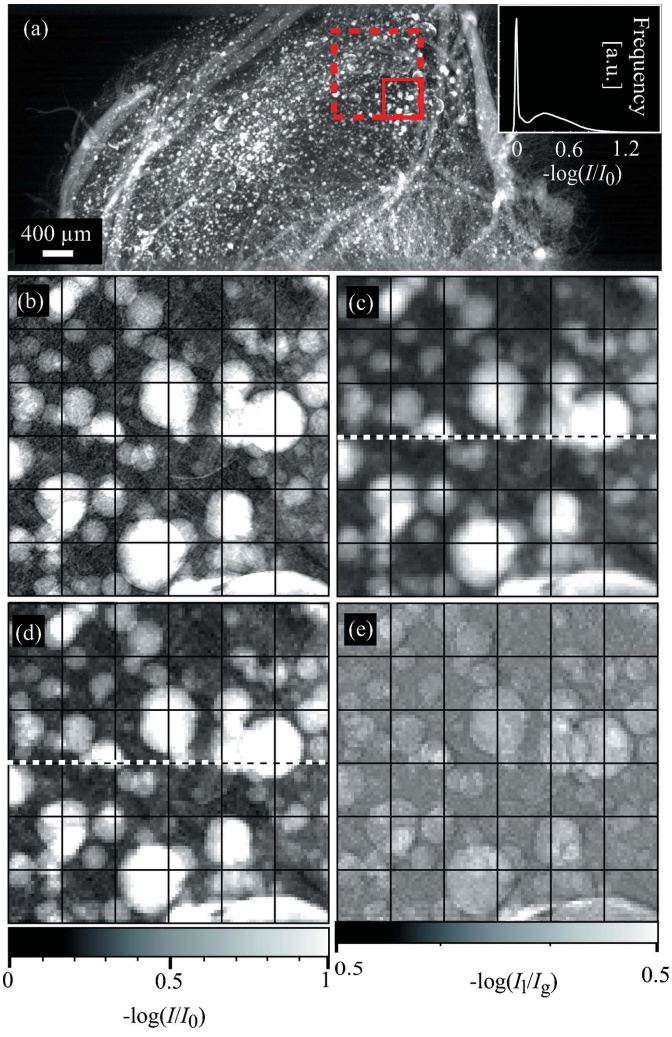

Figure 3
The radiographs of the tumor vessel cast were measured at TOMCAT beamline (SLS at Paul Scherrer Institute, Villigen, Switzerland): (*a*) global radiograph with a pixel size of 5.92 µm; the dashed-line rectangle illustrates the region measured for local tomography with a pixel size of 0.74 µm; the full-line rectangle denotes the region of interest shown in the other images: (*b*) radiograph of local tomography using a pixel size of 0.74 µm, (*c*) cropped area from global radiograph, (*d*) re-sampled image from local radiograph; (*e*) difference image between the global projections (I_g) and re-sampled local projection (I_l) to reveal their intensity differences. The 100 µm grids are incorporated as guidelines.

3. Results

3.1. Differences between global and local radiographs

Fig. 3(*a*) shows a characteristic global radiograph (pixel size 5.92 µm). The dashed rectangle represents the region used for local tomography. The full-line rectangle indicates the selected ROI. The radiographs depicted in Figs. 3(*b*)–3(*e*) correspond to this ROI and contain grids as guidelines. The radiograph in Fig. 3(*b*) corresponds to the local projection (pixel size 0.74 µm). The related down-sampled radiograph using a factor of 8.11 is shown in Fig. 3(*d*). The factor of 8.11 originates from the scaling of the rigid registration with the global data. Fig. 3(*c*) is the cropped part of the global projection as given in the full-line rectangle. The image in Fig. 3(*e*) shows the difference image between the global and the down-sampled local projection. In order to obtain a more detailed understanding of the differences between global and local radiographs, their histograms and selected line profiles are displayed in Fig. 4. The histograms and line profiles originate from the data shown in Figs. 3(*c*) and 3(*d*). The locations of the profiles are denoted using the dashed lines in Fig. 3. Both diagrams confirm the 35% higher I/I_0-range in intensity for the local data. As expected, the profile of the local projection shows more details.

3.2. Analysis of the flat-field images

The flat-field images (see Fig. 5) show the typical stripes that come from the multilayer monochromator (Rack *et al.*, 2010). The signal intensity in these raw data describes the number of X-ray photons which have been converted into visible light and recorded by the CCD camera. The entity in which the signal is measured is called the analogue-to-digital unit (ADU).

The signal is much lower in the global image (Fig. 5*a*) than in the local image (Fig. 5*b*). The flat-field image in Fig. 5(*b*) is down-sampled using the factor of 8.11 to obtain the same number of pixels in the two images. The vertical profiles along the dashed lines in the images show the quantification of the

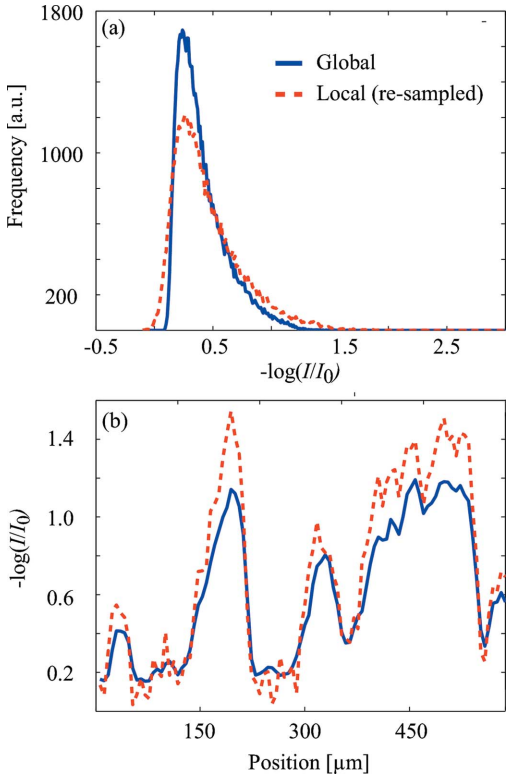

Figure 4
(*a*) The histograms of the global radiographs (blue full line) and of the local radiographs (red dashed line) are obtained from the ROI in Fig. 3. (*b*) The line profiles denoted by the dashed lines in Fig. 3 also show that the dynamic range of the local radiographs is about 30% larger with respect to the global data.

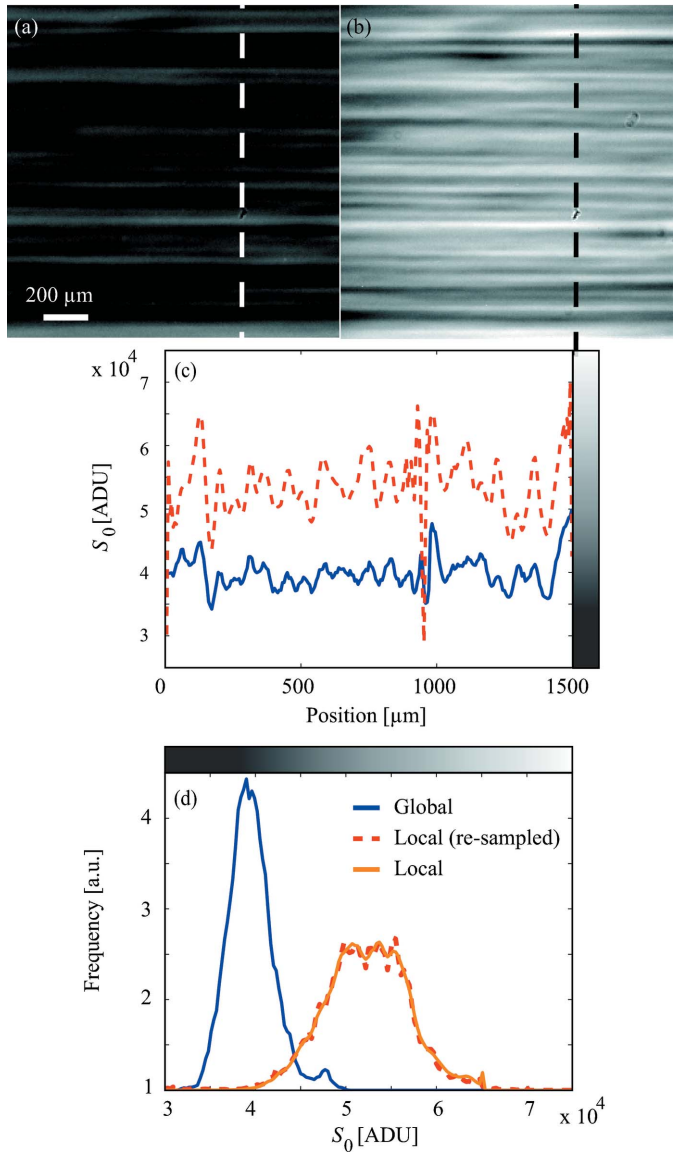

Figure 5
The flat-field images with low-magnifying objective, pixel size 5.92 µm, and high-magnifying objective, pixel size 8.11 × 0.74 µm, reveal an intensity ratio according to the numerical apertures of 0.7, which is close to the expected value of 66/100. See text for details.

observed intensity differences and are shown as examples in Fig. 5(*c*). The related histograms of the two-dimensional images shown in Fig. 5(*d*) differ in peak position by 34% and in FWHM by 75%. The incident photon flux and exposure times per detector frame and the CCD as well as the scintillator used for both measurements were identical, so that the differences must be attributed to the detector lens optics. Indeed, these differences can be quantitatively explained from the different magnifications and numerical apertures of the microscope objectives used (see below) and should be fully eliminated as a result of flat-field corrections.

The ADUs of the re-sampled local flat-field image show visible over-saturation by 9.3%. The maximal ADU value in the non-re-sampled local flat-field image is 0.5% below the saturation limit.

3.3. Absorption histograms of global and local tomography slices

Fig. 6(*a*) shows a selected slice of global tomography from the tumor cast. The dashed circle encloses an area imaged in local tomography. The local region has been found in the global tomograms by 3D registration. The area within the square is presented in Fig. 6(*c*) as cropped, in Fig. 6(*d*) as a local tomography slice re-sampled prior to reconstruction using the scaling factor of 8.11, and in Fig. 6(*e*) as a high-resolution local tomography slice. The incorporated grids validate the appropriate registration. The differences between the images are properly reflected by the histograms in Fig. 6(*b*). The histogram of the local tomography slices is remarkably broader than that of the global data. Even more important, there are substantial shifts of the peak positions to higher X-ray absorption coefficients.

Comparing the two histograms of local tomography one recognizes that the re-sampling has caused a 57% reduction of the FWHM of the air peak close to $\mu = 0$. Such a reduction is the result of the large re-sampling factor and the associated binning (Thurner *et al.*, 2004). The second peak located between 10 and 20 cm^{-1} originates from the Os-loaded polyurethane. There is a third peak above 60 cm^{-1} [not shown in Fig. 6(*b*), see Table 1] which stems from remaining bone (also

Table 1
Selected parameters of the histogram analysis.

	Position of the air peak (cm^{-1})	FWHM of the air peak (cm^{-1})	Distance between air peak and bone peak (cm^{-1})
Global tomogram	$0.00 \pm 3 \times 10^{-13}$	0.52 ± 0.0001	61.7 ± 0.2
Local tomogram	2.74 ± 0.02	5.85 ± 0.02	84.5 ± 0.3
Global tomogram from incomplete data	1.27 ± 0.02	0.89 ± 0.02	63.5 ± 0.3
Re-sampled local tomogram	2.56 ± 0.05	5.71 ± 0.02	84.6 ± 0.4
Local tomogram after de-cupping	0.54 ± 0.03	4.33 ± 0.03	66.9 ± 0.5
Re-sampled histogram matched local tomogram	1.68 ± 0.02	1.51 ± 0.02	54.9 ± 0.5
Histogram matched local tomogram	1.91 ± 0.02	3.90 ± 0.02	54.6 ± 0.3
Re-sampled local tomogram with missing data	0.27 ± 0.01	2.18 ± 0.01	85.0 ± 0.1
Local tomogram with missing data	0.31 ± 0.02	4.90 ± 0.02	83.2 ± 0.4

Os-loaded) and relates to the bright clusters in the tomography slices.

3.4. Absorption histograms of global and local tomograms

Fig. 7 compares the absorption histograms of the 3D datasets. Fig. 7(*a*) shows the effect of re-sampling using the scaling factor 8.11. As already recognized for the two-dimensional data, the re-sampling gives rise to significantly sharper peaks.

It is reasonable to analyze the effect of local reconstruction in the absence of the differences in the optics. This can be achieved by truncating the ROI from the global projections before reconstruction is carried out. In Fig. 7(*b*) the histograms of the globally acquired images, where ROI cropping took place after (blue full line) and before (red dashed line) reconstruction, are shown. The locally reconstructed data are slightly shifted to higher absorption coefficients and exhibit significant peak broadening. Nevertheless, peak shift and broadening are much less pronounced than for the locally acquired data.

3.5. Correcting local tomograms using histogram matching

Local tomography does not often provide the correct local X-ray absorption coefficients (*cf.* Fig. 7). Therefore, the application of histogram matching, well known from image processing, to adjust the histograms of two images (Gonzalez & Woods, 2002) might be an appropriate approach for correcting the local X-ray absorption coefficients. In order to keep the procedure simple, we suggest not directly modifying the tomograms but the radiographs. However, we use a simplified approximation to histogram matching that uses only two scalar parameters and approximates the two histograms by stretching and shifting one of them. As shown in Fig. 4(*a*), the histograms of the radiographs exhibit just one peak of different FWHM. To equate the FWHM of the re-sampled local data to that of the global histogram, the intensity values for every locally acquired and re-sampled radiograph $I(x,y)$ is corrected using the difference between the most frequently occurring intensity value in the global projection and in the local projection D, and the ratio of the FWHMs R,

$$I_{\rm HM}(x, y) = R[I(x, y) - 1] - D. \quad (5)$$

Based on the corrected radiographs $I_{\rm HM}(x,y)$, tomograms were reconstructed and their histograms compared with the histograms of the original datasets. As displayed in Fig. 8, this histogram-matching

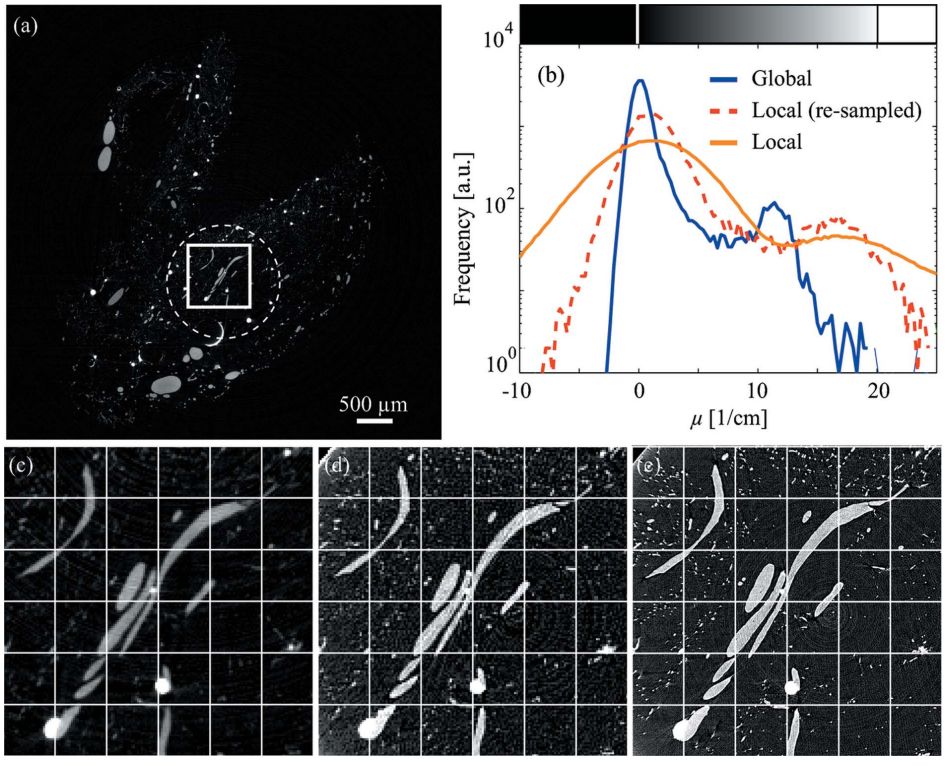

Figure 6
The tomography slice (*a*) is globally acquired (5.92 µm) and shows a virtual cut through the entire tumor. The dashed circle encloses the locally acquired tomogram (0.74 µm). The full-line rectangle corresponds to the cropped area (*c*), the tomography slice of the local tomography, re-sampled using the factor 8.11 (*d*), and with high spatial resolution (*e*). The related histograms of the slices (*b*) show the massive influence of the different analyses on the local X-ray absorption coefficients.

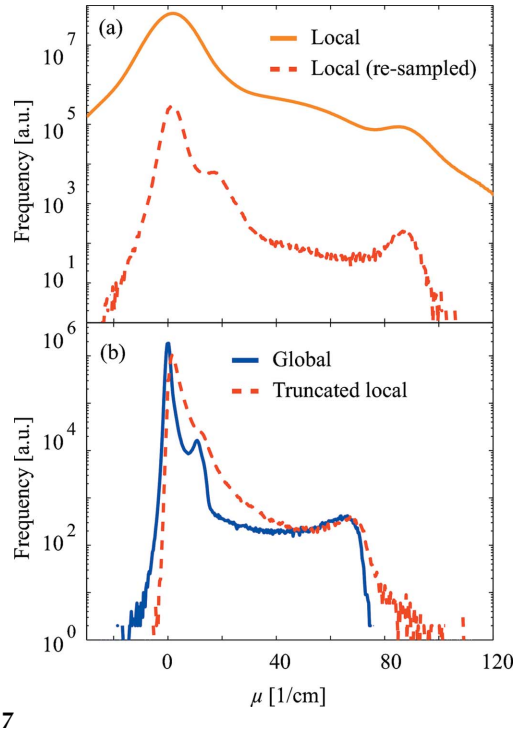

Figure 7
Histograms of the 3D data: (*a*) the influence of re-sampling the local data using the factor 8.11; (*b*) cropping globally acquired data before (red dashed line) and after (blue full line) reconstruction.

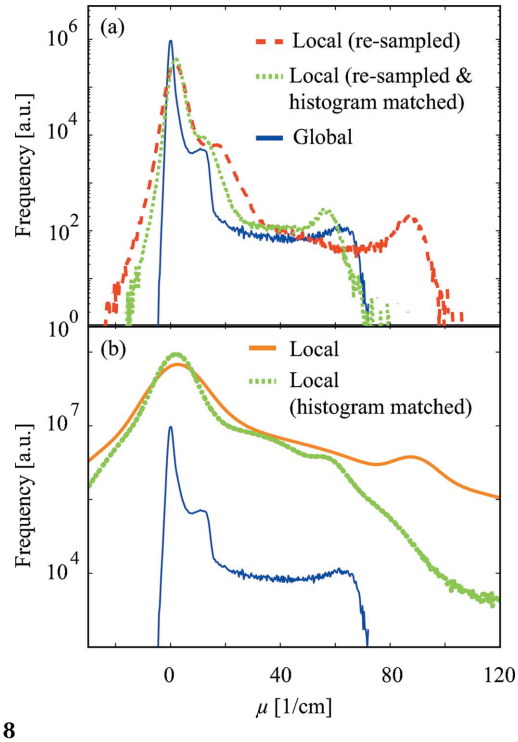

Figure 8
Correcting local radiographs using histogram matching: (*a*) histograms of re-sampled tomography data and (*b*) histograms of high-resolution tomography data.

procedure of the locally acquired data causes a significant peak sharpening and peak shifts to more reliable absorption coefficients. The sharpening in the histograms of the radiographs by 35% reduces the FWHM of the air peak by 25% for the local re-sampled tomogram and 33% for the local tomogram. Nonetheless, the air-related peak in the corrected histograms is still well above zero.

3.6. Extending local sinograms by less detailed global data

In order to complete the local projections, one may take advantage of the less detailed global projections. Because the local and global projections have different pixel sizes, the local projections were down-sampled using the factor of 8.11. The regions in the global projections showing the identical regions visible in the local ones were replaced by the down-sampled local projections with a precision in pixel size of 5.92 µm. Fig. 9(*a*) shows a comparison of the histograms of the tomography data with and without such an extension. The extensions of the re-sampled local projections by the less detailed global ones lead to a slight shift to smaller absorption coefficients.

Alternatively, one can up-sample the global projections to fit the pixel size of the local data. This approach, however, yields huge datasets. Fig. 9(*b*), therefore, shows the histograms of only one tomography slice. Again, the extension slightly shifts the peaks to more reasonable X-ray absorption coefficients. Unfortunately it coincides with a significant broadening of the peaks.

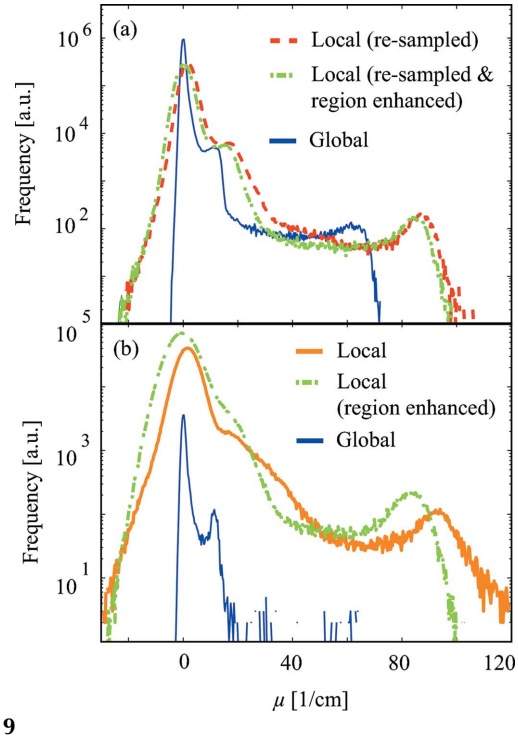

Figure 9
Extending local sinograms by less detailed global data: (*a*) histograms of re-sampled tomography data and (*b*) histograms of high-resolution tomography data.

3.7. Empirical cupping correction

Cupping artifacts occur in cone-beam computed tomography and result from beam hardening (Kak & Slaney, 1988).

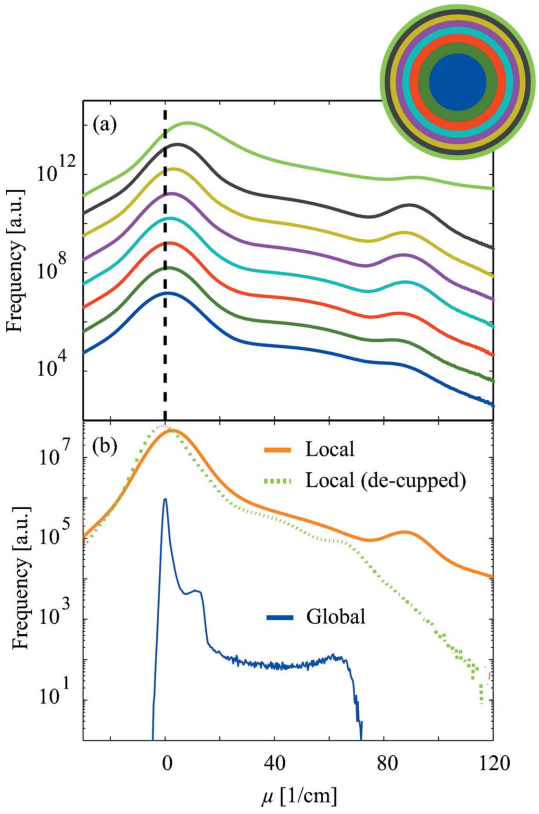

Figure 10
Empirical cupping correction of tomography data: (*a*) histograms of color-coded regions with the same number of voxels (the lower histogram relates to the central sub-domain and the upper histogram to the peripheral sub-domain); (*b*) histogram modification as the results of the cupping correction by means of the air peak shift.

Although the origin of beam hardening is quite different, a similar behavior could be identified in the local tomograms presented here [*cf.* Fig. 10(*a*)]. It was communicated (Schneider *et al.*, 2009; Weitkamp *et al.*, 2002) that the absorption peaks shift to larger absorption coefficients from the rotation center to the periphery. Thus, the tomogram was divided into eight concentric sub-domains of identical area as illustrated for one slice in Fig. 10. For each of the color-coded 3D subunits the histogram is plotted. The air peaks show larger shifts to higher X-ray absorption coefficients for larger distance to the center of the local tomogram. Although this order is not found for the bone peak, absorption coefficient shifts for the different distances to the rotation center have been observed as well. These peak shifts were applied for an empirical cupping correction of the tomography data, which might also be termed 'de-cupping'.

The correction of the histograms includes two components. First, the shift of the air-related peak present in the data of the eight subunits [*cf.* Fig. 10(*a*)] was applied as an individual constant for each subunit to guarantee that the air peaks have their maxima at zero absorption. This procedure, however, shows a non-linear dependence on the distance to the rotation center so that a cubic-spline interpolation of the *Matlab R2010a* code has been applied to achieve a gradual change from center to periphery. Second, the absorption coefficients in the locally acquired data were compressed adapting the peak distances between air and Os-loaded bone to the values of the global tomogram to obtain the bone-related maximum at the desired absorption coefficient.

The resulting histogram is displayed in Fig. 10(*b*). Such an empirical de-cupping, however, only reduces the FWHM of the air peak by 20% and the three peaks are still much broader than the peaks in the global data. While the peaks for air and Os-loaded bone are forced to the absorption coefficients of the global tomogram, the Os-loaded polyurethane peak prominent in the global data is missing in the histograms of the high-resolution data.

3.8. Tumor vessel system

The software *VG Studio MAX 2.0* (Volume Graphics, Heidelberg, Germany) served for the visualization of the tumor vessels. Fig. 11 represents 3D tumor vessel images of global and local data. The high-resolution tomography data were corrected using histogram matching to apply a well comparable threshold for the two images. The high-resolution local data reveal the small capillaries, whereas the global data merely show a non-uniform background. In the majority of cases, however, the authors show images with individually adapted thresholds to avoid such a background and to better highlight certain features. The Os-loaded bone left-overs, for example, are more clearly visible in Fig. 12. The direct comparison of the global with the histogram-matched local tomography data demonstrates that the vast majority of the small capillaries with diameters between 3 and 15 µm are missing in the image of the global data.

4. Discussion

Local tomography provides useful 3D images with a lot of details, but the absorption coefficients obtained from a simple tomographic reconstruction of local tomography data are usually inconsistent with global data, *i.e.* data in which the detector field covers the full width of the specimen. Against that, the global data are generally less detailed. Therefore, in multi-scale studies, it seems attractive to correct the local tomography data by means of the global data. In the present paper we have evaluated three empirical approaches, *i.e.* two-parameter histogram matching, sinogram extension and multi-parameter cupping correction, to identify an effective procedure for correcting the local X-ray absorption coefficients in local tomography data.

The discrepancies between the X-ray absorption coefficients obtained from the local and the global data is, at least partly, due to systematic artifacts, often termed bias, in the local data that result from the fact that the locally acquired projections are truncated (Frese *et al.*, 2003; Hamelin *et al.*, 2010). However, differences in the response functions of the detector configurations used for the acquisitions can be an additional source of discrepancy. Before a direct comparison between local and global tomography, the potential influence of the detector optics should therefore be analyzed and

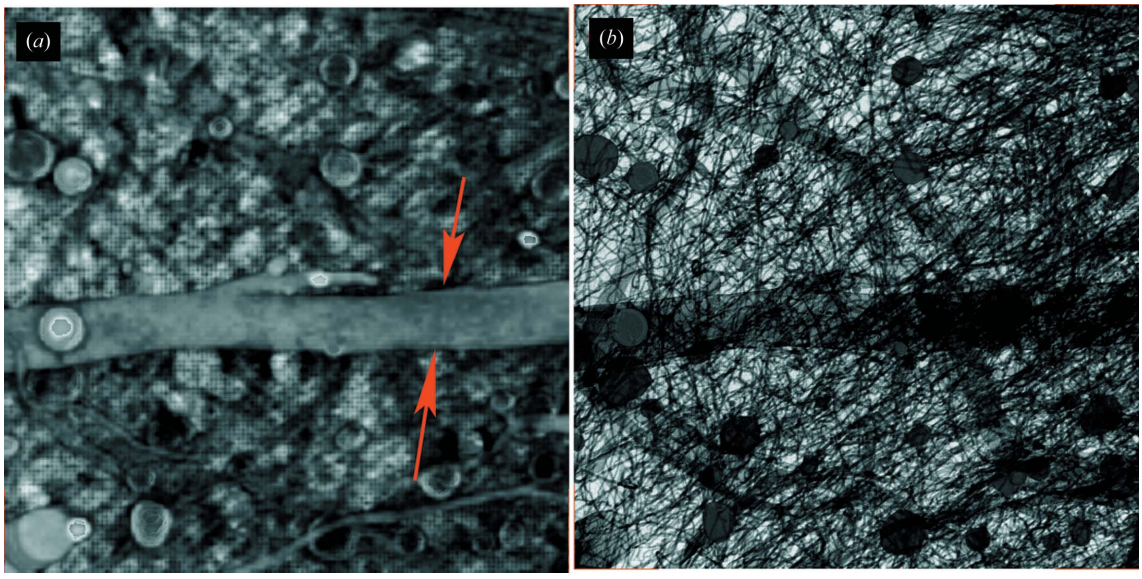

Figure 11
Comparing globally (*a*) and locally (*b*) acquired 3D representations of the tumor vessel system. The histogram matching of the locally acquired data allows an equivalent threshold to be chosen for the local data showing a network of small capillaries and for the global data exhibiting a non-uniform background.

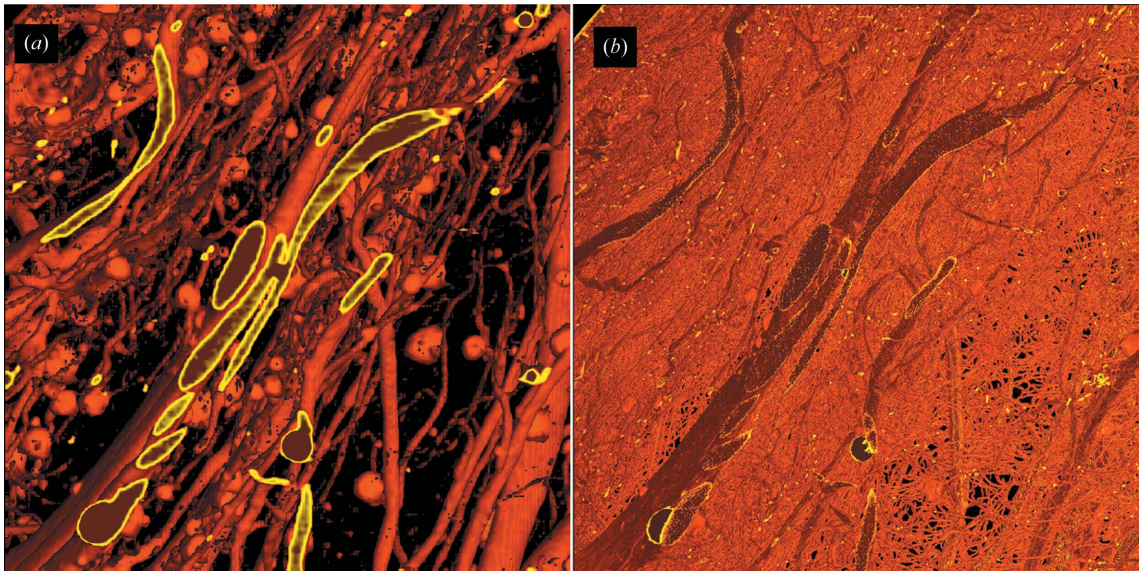

Figure 12
Using different thresholds for global and local data, the dense network of smaller capillaries seen in the histogram-matched local data (*b*) can become completely invisible in the global data (*a*).

suitable registration algorithms with voxel precision have to be employed.

The flat-field images recorded with the 1.25× (NA 0.04) and 10× (NA 0.4) objectives exhibit different brightness. As the numerical aperture differs by a factor of ten and the magnification only by a factor of 8.11, an average signal ratio between the global and the local data of $(8.11/10)^2 = 0.66$ should be expected. This matches the experimentally observed ratio of around 0.7. In any case, this effect should only enter into the statistical noise properties, not into the systematic shift of the reconstructed absorption coefficients, because the radiographs of both data sets were corrected in the conventional manner by subtraction of dark images and normalization to flat-field images taken with the object removed from the beam.

The observed maximal intensity for the re-sampled flat-field images exceeds the limited detector readout of 16-bit by 9.3%. This high value is not related to over-saturation of the detector during acquisition but is caused by re-sampling phenomena.

The rigid registration between the global and re-sampled local radiographs resulted in errors of sub-pixel magnitude. These remaining errors, however, cannot explain the significant discrepancies between the values of global and re-sampled local radiographs, as clearly identified in the images

of Figs. 3 and 4. While a quantitative explanation of this phenomenon is beyond the scope of this study, we attribute the broader histogram of the locally acquired data with respect to the globally acquired ones mainly to the differences in the point-spread function of the imaging system (Martin & Koch, 2006), especially to the tails in this function. This is because other possible contributions are cancelled out by the re-sampling of the high-resolution data to the larger pixel size of the global data. The effects, which the re-sampling procedure eliminates (or drastically reduces), include, in particular, any differences owing to the presence of edge-enhancing phase-contrast fringes in the high-resolution data, as well as the different statistical properties of the two data sets in so far as they are directly caused by the different pixel sizes of the data.

The registration procedure of the radiographs reveals that the agreement between the global and local images is significantly better if the global projections are shifted by two or three angular steps (θ) of the specimen rotation (each step 0.12°) with respect to the local projections. The more reliable 3D-registration procedure of the tomograms corroborates this observation. The related rotation parameter corresponds to $\theta = 0.31°$, whereas no rotational misalignment in the perpendicular directions has been found. Hence, the not exactly adjusted rotation angle gives rise to a misalignment of 0.05° from the third angular step ($\theta = 0.36°$). For the tumor, this angular misalignment may cause errors in intensity of about 1%, but contributes only in a negligible manner to the discrepancies in the histograms mentioned above also because the detector is assumed to work in the linear domain (PCO-AG, 2008). Corrections of systematic errors as proposed by Tsuchiyama *et al.* (2005) cannot be applied, since the exact composition of the specimen is unknown.

One could presume that another source of error may lie in deformations of the highly elastic specimen during the data acquisition. The visible deformation in the projections [see Fig. 3(*e*)], however, corresponds to only 1.2‰ only and can therefore be neglected. In order to exclude any noteworthy deformation during data recording, affine registration including global shearing and variable scaling parameters in the orthogonal directions has been carried out (Modersitzki, 2004). These calculations have not given any indication of such deformations. Therefore, we conclude that the specimen has not changed its shape and relative movement artifacts can be excluded.

The registrations of the radiographs and of the tomograms make available the scaling parameters in the orthogonal directions between global and local data, which correspond to 8.11 ($\pm$0.02). This value is only slightly higher than the nominal one given by the supplier of the objectives (Koch *et al.*, 1998; Martin & Koch, 2006). Variations between the three orthogonal directions of maximal 0.02 are well below the pixel size of the global data.

The absorption histograms of the common volumes of globally and locally acquired data strongly differ regarding absolute and relative peak positions and half widths. The partial volume effects, much stronger in the global tomograms (Müller *et al.*, 2002), and the edge enhancement, more clearly visible in the local tomograms (Snigirev *et al.*, 1995; Thurner *et al.*, 2003, 2004), can notably influence the histograms and explain the main discrepancies between the histograms before re-sampling or binning. As the re-sampling with a factor of about eight equals an averaging, these two effects should be of minor importance comparing the global and the re-sampled local absorption histograms of common volumes. Binning, which corresponds to the use of a large re-sampling factor (here about eight), especially carried out prior reconstruction, significantly sharpens the peaks and thereby improves the contrast (density resolution) (Thurner *et al.*, 2004). Comparison of the histograms obtained from the high-resolution data with the re-sampled local histograms confirms this earlier result.

While the air peak of the global tomography data is detected at X-ray absorption coefficients close to zero (*cf.* Table 1), the air peak of the local data is located at about 2.8 cm^{-1}. A shift to higher X-ray absorption (1.3 cm^{-1}) is also observed if the global data are restricted to the common region with the local radiography for reconstruction. Therefore, in agreement with the literature (Kak & Slaney, 1988), this shift is regarded as an artifact owing to the local acquisition geometry.

Peak broadening in 3D data histograms may originate from minor peak shifts from slice to slice. One of the reasons for these shifts can be the photon energy gradient in X-ray beams from multilayer monochromators. However, in the present case this phenomenon can be excluded as the effect is absent within the global tomogram. For the local data, however, the air peak position scatters around the mean value of 2.76 cm^{-1} by 0.84 cm^{-1}. Correcting this scattering from slice to slice, the FWHM of the air peak does not diminish remarkably (only 0.7%).

In order to reduce the artifacts related to the truncation of the local projections, it seems to be straightforward to complement the local radiographs (or, equivalently, the sinograms) by the less detailed global data that were previously described as zoom-in tomography (Xiao *et al.*, 2007). For the data sets in the present study, however, the results of this approach, given in Fig. 9, are rather disappointing. The peak positions of polymer and bone in the extended local data are only slightly shifted and still far from the peaks derived from the global tomogram. This observation is in quantitative agreement with the simulations and experimental data of Xiao *et al.* (2007). The error estimated on the basis of this approach corresponds to a reduction by 11%, which fits our result of 14%. Therefore, this approach only supports the correction of the air-related peak. The observation that the sinogram extension approach does not yield satisfactory results, and does not have as much effect on the data as would be needed to match the histograms, constitutes strong evidence that, for the present data set, the mismatch in reconstructed absorption coefficients between the local and global data is not primarily due to the typical local-tomography artifacts. Since, in addition, almost all experimental parameters were the same in the acquisition of both data sets, with the only major exception of

the detector configurations used in both data sets, we conclude that the discrepancies are primarily caused by differences in the detector response functions.

Among the model-independent approaches, histogram matching belongs to the powerful methods of matching the data. However, conventional histogram matching is rather difficult for tomography data because of their size, especially since the number of voxels in the common volume differs between the global and local data by a factor of 535. Therefore, we chose the approach of histogram matching of the radiographs prior to reconstruction. Because the intensity histogram of the global data [*cf.* Fig. 4(*a*)] exhibits discontinuities, the conventional histogram-matching procedure has been replaced by a two-parameter approach to generate a distribution with comparable peak position and half-width. This approach does not provide perfect agreement, but much better results than the sinogram extension. Evaluating the graphs in Fig. 8(*a*), it has to be stated that this histogram matching does not yet yield reliable local X-ray absorption coefficients. Therefore, the two-parameter histogram matching of the radiographs is considered to be rather an empirical method. It also may depend on the choice of specimen. In the present example, however, it can be applied to determine a common threshold for the direct comparison of global and local tomography images.

5. Conclusions

Local tomography is a powerful technique for generating 3D pictures of small features in a larger specimen that exhibit a strong X-ray absorption difference compared with their surroundings. The local X-ray absorption coefficients derived from local tomography, however, are only semi-quantitative even after applying correction procedures.

For the two data sets investigated here, the findings from the different approaches used to match the reconstructed values of absorption coefficients, together with the comparison of equivalent regions in the projection data (Fig. 4*b*), brought us to the conclusion that the differences observed in the reconstructed X-ray absorption coefficients in the tomograms are predominantly due to different point-spread functions of the two detector configurations used resulting from the exchange of the lens in front of the camera, and much less to the fact that one of the data sets was acquired in a local geometry. In the present case a simple histogram-stretching method therefore yielded better results to match the reconstructed values than, for example, sinogram extension of the local data by the global data set.

Generally, our study shows that, when attempting to match data sets from multi-scale tomography measurements, experimentalists should not only consider the well known phenomenon of the shift of the reconstructed values owing to local acquisition geometries, but also potential differences owing to other factors, such as different response of the detector configurations used. Beyond the present paper, the question of how far the absorption coefficients obtained by SRμCT, even those obtained in global geometry, are quantitatively correct depends on how much the detector response function, in each individual case, affects the measured I/I_0 values in the normalized projections. For cases where these effects are not negligible, and where quantitatively correct absorption values are needed, well defined and effective calibration protocols may have to be established.

The authors gratefully acknowledge E. Meyer from the Institute of Zoology, University of Zürich, for providing assistance during the corrosion cast, and F. Schmidli who took the photographs of the specimen. We are additionally thanking H. Deyhle for downloading and storing the data. The authors favorably acknowledge the contributions of F. Marone and M. Stampanoni from the Paul Scherrer Institut during data acquisition and for manuscript preparation. The project was partially funded by the Swiss National Science Foundation (200021_127297/1) and was supported by the SLS (proposal 2008959). TW received support from RTRA 'Digiteo' and RTRA 'Triangle de la Physique' (grants 2009-034T and 2009-79D).

References

Andronache, A., von Siebenthal, M., Székely, G. & Cattin, P. (2008). *Med. Image Anal.* **12**, 3–15.
Bonnet, S., Peyrin, F., Turjman, F. & Prost, R. (2000). *IEEE Trans. Image Process.* **9**, 1445–1450.
Faridani, A., Ritman, E. L. & Smith, K. T. (1992). *SIAM J. Appl. Math.* **52**, 1193–1198.
Frese, T., Rouze, N. C., Bouman, C. A., Sauer, K. & Hutchins, G. D. (2003). *IEEE Trans. Med. Imag.* **22**, 1806–1810.
Gonzalez, R. C. & Woods, R. E. (2002). *Digital Image Processing.* New Jersey: Prentice Hall.
Gureyev, T., Nesterets, Y. & Mayo, S. (2007). *Opt. Commun.* **280**, 39–48.
Haberthür, D., Hintermüller, C., Marone, F., Schittny, J. C. & Stampanoni, M. (2010). *J. Synchrotron Rad.* **17**, 590–599.
Hamelin, B., Goussard, Y., Dussault, J.-P., Cloutier, G., Beaudoin, G. & Soulez, G. (2010). *Med. Phys.* **37**, 4577–4589.
Hammersley, A. P. (1999). *PyHST*, http://www.esrf.eu/computing/scientific/HST/HSTREF/hst.html.
Kak, A. C. & Slaney, M. (1988). *Principles of Computerized Tomographic Imaging.* New York: IEEE Press.
Knops, Z. F., Maintz, J. B., Viergever, M. A. & Pluim, J. P. (2006). *Med. Image Anal.* **10**, 432–439.
Koch, A., Raven, C., Spanne, P. & Snigirev, A. (1998). *J. Opt. Soc. Am.* **15**, 1940–1951.
Köhler, T. & Noo, F. (2009). *Phys. Rev. Lett.* **102**, 1.
Krucker, T., Lang, A. & Meyer, E. P. (2006). *Microsc. Res. Tech.* **69**, 138–147.
Kudo, H., Courdurier, M., Noo, F. & Defrise, M. (2008). *Phys. Med. Biol.* **53**, 2207–2231.
Marone, F., Münch, B. & Stampanoni, M. (2010). *Proc. SPIE*, **7804**, 780410.
Martin, T. & Koch, A. (2006). *J. Synchrotron Rad.* **13**, 180–194.
Modersitzki, J. (2004). *Numerical Methods for Image Registration.* Oxford University Press.
Müller, B., Beckmann, F., Huser, M., Maspero, F., Székely, G., Ruffieux, K., Thurner, P. & Wintermantel, E. (2002). *Biomol. Eng.* **19**, 73–78.
Müller, B., Bernhardt, R., Weitkamp, T., Beckmann, F., Bräuer, R., Schurigt, U., Schrott-Fischer, A., Glueckert, R., Ney, M., Beleites, T., Jolly, C. & Scharnweber, D. (2007). *Intl J. Mater. Res.* **7**, 613–621.

Müller, B., Lang, S., Dominietto, M., Rudin, M., Schulz, G., Deyhle, H., Germann, M., Pfeiffer, F., David, C. & Weitkamp, T. (2008). *Proc. SPIE*, **7078**, 70780B.
PCO-AG (2008). *pco.2000*, http://www.pco.de/fileadmin/user_upload/db/products/datasheet/pco2000_20080805.pdf.
Pfeiffer, F., David, C., Bunk, O., Donath, T., Bech, M., Le Duc, G., Bravin, A. & Cloetens, P. (2008). *Phys. Rev. Lett.* **101**, 168101.
Potter, R. F. & Groom, A. C. (1983). *Microvasc. Res.* **25**, 68–84.
Rack, A., Weitkamp, T., Riotte, M., Grigoriev, D., Rack, T., Helfen, L., Baumbach, T., Dietsch, R., Holz, T., Krämer, M., Siewert, F., Meduňa, M., Cloetens, P. & Ziegler, E. (2010). *J. Synchrotron Rad.* **17**, 496–510.
Schneider, P., Voide, R., Stampanoni, M. & Müller, R. (2009). *Biomed. Tech/Biomed. Eng.* **54**, 48–54.
Snigirev, A., Snigireva, I., Kohn, V., Kuznetsov, S. & Schelokov, I. (1995). *Rev. Sci. Instrum.* **66**, 5486–5492.
Stampanoni, M., Groso, A., Isenegger, A., Mikuljan, G., Chen, Q., Bertrand, A., Henein, S., Betemps, R., Frommherz, U., Bohler, P., Meister, D., Lange, M. & Abela, R. (2006). *Proc. SPIE*, **6318**, 63180M.
Takeda, T., Itai, Y., Hyodo, K., Ando, M., Akatsuka, T. & Uyama, C. (1998). *J. Synchrotron Rad.* **5**, 326–332.
Thurner, P., Beckmann, F. & Müller, B. (2004). *Nucl. Instrum. Methods Phys. Res. B*, **225**, 599–603.
Thurner, P., Müller, B., Beckmann, F., Weitkamp, T., Rau, C., Müller, R., Hubbell, J. A. & Sennhauser, U. (2003). *Nucl. Instrum. Methods Phys. Res. B*, **200**, 397–405.
Tsuchiyama, A., Uesugi, K., Nakano, K. & Ikeda, S. (2005). *Am. Mineral.* **90**, 132–142.
Weitkamp, T., Rau, C., Snigirev, A. A., Benner, B., Günzler, T., Kuhlmann, M. & Schroer, C. G. (2002). *Proc. SPIE*, **4503**, 92–102.
WHO (2009). *Cancer*, http://www.who.Int/mediacentre/factsheets/fs297/en/index.html.
Wiedeman, M. P. (1963). *Am. Heart Assoc.* **12**, 375–378.
Xiao, X., De Carlo, F. & Stock, S. (2007). *Rev. Sci. Instrum.* **78**, 1–7.